remote sensing

Article

Estimates of Daily Evapotranspiration in the Source Region of the Yellow River Combining Visible/Near-Infrared and Microwave Remote Sensing

Rong Liu [1], Jun Wen [2,*], Xin Wang [1], Zuoliang Wang [1], Yu Liu [1] and Ming Zhang [3]

[1] Key Laboratory of Land Surface Process and Climate Change in Cold and Arid Regions, Northwest Institute of Eco-Environment and Resources, Chinese Academy of Sciences, Lanzhou 730000, China; rliu@lzb.ac.cn (R.L.); wangxin@lzb.ac.cn (X.W.); zuoliangwang@lzb.ac.cn (Z.W.); yliu@lzb.ac.cn (Y.L.)
[2] College of Atmospheric Sciences, Chengdu University of Information Technology, Chengdu 610225, China
[3] Faculty of Geomatics, East China University of Technology, Nanchang 330013, China; 200160008@ecut.edu.cn
* Correspondence: jwen@cuit.edu.cn

Abstract: The spatial variation of surface net radiation, soil heat flux, sensible heat flux, and latent heat flux at different times of the day over the northern Tibetan Plateau were estimated using the Surface Energy Balance System algorithm, data from the FY-2G geostationary meteorological satellite, and microwave data from the FY-3C polar-orbiting meteorological satellite. In addition, the evaporative fraction was analyzed, and the total evapotranspiration (ET) was obtained by the effective evaporative fraction to avoid the error from accumulation. The hourly change of latent heat flux presented a sound unimodal diurnal variation. The results showed the regional ET ranged between 2.0 and 4.0 mm over the Source Region of the Yellow River. The conditional expectations of surface energy components during the experimental period of the study area were statistically analyzed, and the correspondence between different surface temperatures and the effective energy distribution was examined. The effective energy distribution of the surface changed significantly with the increase in temperature; in particular, when the surface temperature exceeded 290 K, the effective energy was mainly used for surface ET. The aim of this study was to avoid the use of surface meteorological observations that are not readily available over large areas, and the findings lay a foundation for the commercialization of land surface evapotranspiration.

Keywords: visible and near-infrared; microwave; evapotranspiration; FengYun meteorological satellite; evaporation fraction; Source Region of the Yellow River

Citation: Liu, R.; Wen, J.; Wang, X.; Wang, Z.; Liu, Y.; Zhang, M. Estimates of Daily Evapotranspiration in the Source Region of the Yellow River Combining Visible/Near-Infrared and Microwave Remote Sensing. *Remote Sens.* **2021**, *13*, 53. https://dx.doi.org/10.3390/rs13010053

Received: 19 November 2020
Accepted: 24 December 2020
Published: 25 December 2020

1. Introduction

The variation of regional evapotranspiration is of significance for the land surface process and the energy exchanges in the hydrosphere, atmosphere, and biosphere [1–3]. Due to the development of observation methods and understanding of the turbulence process in the atmospheric boundary layer, the method of calculating land surface evapotranspiration has gradually developed from the traditional spot-measurements-based method to regional evapotranspiration estimation based on the technology of large-scale satellite remote sensing [4].

Since the mid-1970s, numerous scholars have undertaken a large amount of research on the accuracy of evapotranspiration retrieved by remote sensing [5,6]. According to different theories, remote sensing evapotranspiration models can be roughly divided into three categories. First category is based on the Penman-Monteith algorithm with an improvement of its parameters, using remote sensing data and ground observation data to estimate the actual evapotranspiration [7]. The second type is a statistical empirical model, which attempts to establish a correlation between evapotranspiration and vegetation index (VI) or surface-air temperature difference [8,9], or derives the two-dimensional scatter diagram of land surface temperature and vegetation index (or albedo) with specific trapezoidal or triangular characteristics [10,11]. The third category comprises the single and dual-source models based on the principle of energy balance, among which the Surface Energy Balance Algorithm for Land (SEBAL) model [12], Simplified Surface Energy Balance Index (S-SEBI) model [13], Surface Energy Balance System (SEBS) model [14], and Mapping Evapotranspiration with Internalized Calibration (METRIC) model [15] are the typical cases of a single-source model while Shuttleworth-Wallace model [16] and N95 model [17] are dual-source models.

The Qinghai-Tibet Plateau has an average altitude of more than 4000 m, accounting for a quarter of China's total land area, and is an important source of water and heat for the East Asian monsoon circulation. Its huge topography and unique geographical location determine that its surface evapotranspiration not only plays an important role in the formation and evolution of the Asian monsoon system but is also closely related to changes in regional surface water resources over the Qinghai-Tibet Plateau. The temperature data of 50 meteorological stations on the Qinghai-Tibet Plateau from the 1950s to the 1990s showed that both the temperature and precipitation of the Qinghai-Tibet Plateau have displayed a significant upward trend [18]. Therefore, evapotranspiration, which is the main process of water loss, is closely related to the changes in water resources over the Qinghai-Tibet Plateau.

However, the visible and near-infrared observation of sensors fails in cloud-covered conditions. Hence, for evapotranspiration estimates, most of the models noted above based on satellite remote sensing avoid cloud cover and use observation data provided by polar-orbiting satellites to estimate the instantaneous latent heat flux as the sensor passes. In this process, errors cannot be avoided and the diurnal variation process of the evapotranspiration cannot be obtained. Alternatively, geostationary meteorological satellites can provide high-frequency observation data once per hour, allowing the real-time monitoring of the regional surface state, and the microwave radiometer carried by these satellites can penetrate clouds and fog to retrieve the surface flux under cloud-cover conditions. However, the regional evapotranspiration combined with two kinds of data is not commonly studied.

The Source Region of the Yellow River (SRYR) is located in the northeast of the Tibetan Plateau. As an important runoff of the Yellow River, the SRYR area supplies about 45.0% of the water in the upper reaches of the Yellow River, and is thus also called "the Reservoir of the Yellow River" [18]. In this study, the spatial distributions of the hourly surface net radiation, soil heat flux, latent heat flux, and sensible heat flux in the SRYR area were estimated using observations from the FY-2G geostationary meteorological satellite and SEBS model in real-time. During afternoons, when the plateau convective cloud develops vigorously, MicroWave Radiation Imager (MWRI) data from the FY-3C polar-orbiting meteorological satellite was used to obtain the surface energy fluxes. The results were verified with the observation data from the Source Region of the Yellow River Alpine Climate Station. The statistical results and errors were also analyzed, and are discussed in the current paper. This paper intends to provide more reliable results for evapotranspiration in typical summer weather in the SRYR area.

The paper is organized as follows: In Section 2 the methodology is briefly described. The study area and observation data are presented in Section 3. Section 4 presents results and verification. Finally, a discussion and conclusions of this study are presented in Sections 5 and 6, respectively.

2. Methodology

2.1. Net Radiation

2.1.1. Net Radiation under Clear Sky Conditions

Cloud classification and cloud total amount of products obtained from the FY-2G geostationary meteorological satellite can determine whether the grid point is covered with clouds. When the cloud classification product is defined as the clear sky and the cloud total amount is less than 10%, it is considered to be a clear sky condition (no clouds) and the near-surface net radiation R_n is calculated according to:

$$R_n = (1 - \alpha)Q + L\downarrow - L\uparrow \tag{1}$$

where, α is the surface albedo, determined by MODIS observation data; Q is the total solar radiation, including direct radiation, scattered radiation, and reflected radiation [19].

$L\downarrow$ is the downward long-wave radiation, which can be obtained by:

$$L\downarrow = \varepsilon_a \cdot \sigma \cdot T_a^4 \tag{2}$$

where, ε_a is the air effective emissivity, obtained from actual water vapor pressure and air temperature [20]; σ is the Stefan-Boltzman constant, which is 5.669 $\times$ 10^{-8} $\mathrm{Wm}^{-2}\mathrm{k}^{-4}$; T_a is the measured air temperature.

$L\uparrow$ is the upward long-wave radiation, which can be calculated from the formula:

$$L\uparrow = \varepsilon \cdot \sigma \cdot T_s^4 \tag{3}$$

where, ε is the land surface emissivity, obtained by the methods of Chen et al. [19]; T_S is the surface skin temperature, which can be obtained using the Black Body Temperature (TBB) data observed by the Visible Infrared Spin Scan Radiometer (VISSR) on FY-2G and the MODerate resolution atmospheric TRANsmission model (MODTRAN). Specifically, the band response functions of MODTRAN and VISSR are adopted to calculate the atmospheric thermal infrared transmittance and atmospheric thermal infrared radiance. Then, brightness temperature from VISSR thermal infrared band-1 and band-2 are chosen in the surface radiation transfer model. Finally, the results can be derived using an iterative algorithm.

2.1.2. Net Radiation under Cloud Cover

The SRYR is located in the northeast of the Qinghai-Tibet Plateau. The development of convective clouds over the plateau in the summer afternoon limits visible and near-infrared remote sensing. Therefore, a simplified parameterization scheme of surface radiation flux [21] was adopted under cloud-cover conditions. This scheme assumes that the long-wave radiations are approximately equal under cloud cover.

(1) Atmospheric attenuation

The attenuation effect of the atmosphere on solar radiation can be presented by the transmittance τ:

$$\tau = \frac{Q_E}{Q_0} \tag{4}$$

where, Q_E is the solar radiation that reaches the surface after atmospheric attenuation; Q_0 is the total solar radiation at the top of the atmosphere.

(2) The energy received by the satellite sensor

The energy received by the satellite sensor can be divided into two parts: one is the energy of solar radiation that has not been attenuated by the atmosphere, and the other is the energy that reaches the surface after atmospheric attenuation and is reflected [21].

$$\alpha_{TOA} Q_0 = Q_0 \tau \alpha_s \tau + (1 - \tau) Q_0 \tag{5}$$

where, α_{TOA} is the albedo of the top cloud, $\alpha_{TOA}Q_0$ is the energy received by the sensor; α_s is the surface albedo; Q_0 τ α_s τ is the energy passing to the surface after atmospheric attenuation, and reflected and attenuated by the surface; $(1 - \tau)Q_0$ is the energy reflected at the cloud top. Using Equation (5), the formula of atmospheric transmittance can be given by the following:

$$\tau = \frac{1 - \sqrt{1 - 4\alpha_S(1 - \alpha_{TOA})}}{2\alpha_S} \tag{6}$$

where α_{TOA} and α_s are taken from the observations of the geostationary and polar-orbiting satellites, respectively.

The hourly temporal scale transmittance can be derived from Equation (6), and the net radiation calculation formula under the cloudy condition is:

$$Q_E = (1-\alpha)Q_0\tau \tag{7}$$

It should be noted that the atmospheric transmittance obtained from the above formula is not the complete atmospheric transmittance of solar radiation, but the total equivalent extinction effect of the earth-atmosphere system on the radiation transfer path from outside the atmosphere to the ground surface. It represents the interaction between absorption and scattering effects. For satellite sensor observations that are missing or with obviously wrong values, we established the relationship between solar short-wave radiation and solar radiation before the atmospheric effect to calculate the atmospheric transmittance.

2.2. Soil Heat Flux

The formula for soil heat flux is given by:

$$G_o = R_n[\Gamma_c + (1-\mathrm{f}_v)(\Gamma_s - \Gamma_c)] \tag{8}$$

where, Γ_c and Γ_s represent the ratios between G_0 and R_n with 100% vegetation cover and bare soil area. Vegetation coverage follows $f_v = \frac{NDVI - NDVI_{\min}}{NDVI_{\max} - NDVI_{\min}}$, where $NDVI_{min}$ is the normalized difference vegetation index of the bare soil surface, and $NDVI_{max}$ is the normalized difference vegetation index when the area is fully covered with vegetation [21].

2.3. Calculation Method of Sensible Heat Flux

An iterative method is adopted to calculate the sensible heat flux and the specific calculation formula is as follows:

$$u = \frac{u_*}{k}[\ln(\frac{Z-d_o}{Z_{om}}) - \psi_m(\frac{Z-d_o}{L}) + \psi_m(\frac{Z_{om}}{L})] \tag{9}$$

$$\theta_o - \theta_a = \frac{H}{ku_*\rho C_p}[\ln(\frac{Z-d_o}{Z_{oh}}) - \psi_h(\frac{Z-d_o}{L}) + \psi_h(\frac{Z_{oh}}{L})] \tag{10}$$

$$L = -\frac{\rho C_p u_*^3 \theta_v}{kgH} \tag{11}$$

where Z is the height of the reference surface, u is the wind speed, u_* is the friction wind speed, d_o is the zero-plane displacement height, and Z_{om} and Z_{oh} denote momentum and thermal roughness lengths, respectively. ψ_m and ψ_h are the stability correction functions for dynamic and thermodynamic transfer, respectively; θ_o and θ_a are the potential temperature of the surface air and the potential temperature of the reference height, respectively; H is the sensible heat flux; L is the Obukhov length; k is the von Kármán constant; ρ is the air density, C_p is the gas constant; g is the acceleration of gravity; and θ_v is the virtual potential temperature near the surface. More parameters can be seen in Su [14]. The Leaf Area Index (LAI) needed for the calculation of Z_{oh} and Z_{om} can be derived from the method of Chen et al. [19].

In this research, the 37 GHz vertically polarized brightness temperature from the MWRI on the FY-3C polar-orbiting meteorological satellite was used to retrieve the surface temperature under cloud-cover conditions at 16:00 [22].

2.4. Evaporation Fraction

The evaporation fraction is the ratio of actual ET to effective energy (the difference between net radiation and soil heat flux) and can be presented as

$$EF = \frac{LE}{R_n - G_0} \tag{12}$$

where EF is the evaporation fraction, LE is the latent heat flux, R_n is the net radiation flux, and G is the soil heat flux.

The SEBS model defines the limit cases as deficient and sufficient [23]. Since evaporation fraction is stable during the whole day, if we know the net radiation and soil heat flux at a certain time, then the latent heat flux at that time can be calculated using the latent heat of vaporization (2.49×10^6 $\mathrm{Wm^{-2}mm^{-1}}$).

2.5. Validation

Ground observations from the regular meteorological station and eddy covariance system from the SRYR Alpine Climate Station (102°08′ E, 33°53′ N, 3443 m) were used to validate the instantaneous heat fluxes that were estimated from remote sensing retrievals from 1–30 August 2019. The statistical analysis using the root mean square error is also presented in Section 4.2.

Since the soil heat flux observation was at 10 cm, we used the Averaging Soil Thermocouple Probe (TCAV) method to elicit the surface soil heat flux through soil heat storage, which was obtained from the average soil temperature [24]. The daily average soil volumetric water content of 0–10 cm at the observation site was 0.39, and the average porosity of shallow soil was 0.50.

3. Study Area and Observation Data

The source region of the Yellow River is located in the northeastern part of the Qinghai-Tibet Plateau (95.5° E–103.5° E, 31.5° N–36.5° N), with an area of about 1.22×10^5 km^2, accounting for 16% of the total area of the Yellow River Basin. This area, mostly with an altitude of above 4000 m, is mainly covered with alpine meadows (Figure 1). The source region of the Yellow River is located in the "arid-semi-arid" transition zone between the Qinghai-Tibet Plateau and the Loess Plateau. It has a typical continental alpine climate with an average annual temperature of 2.9 °C. Precipitation is mainly concentrated in the period from May to September, accounting for more than 80% of the total, which is 560 mm per year (1956–2016). The annual evaporation is 920 mm, gradually decreasing from southeast to northwest [21].

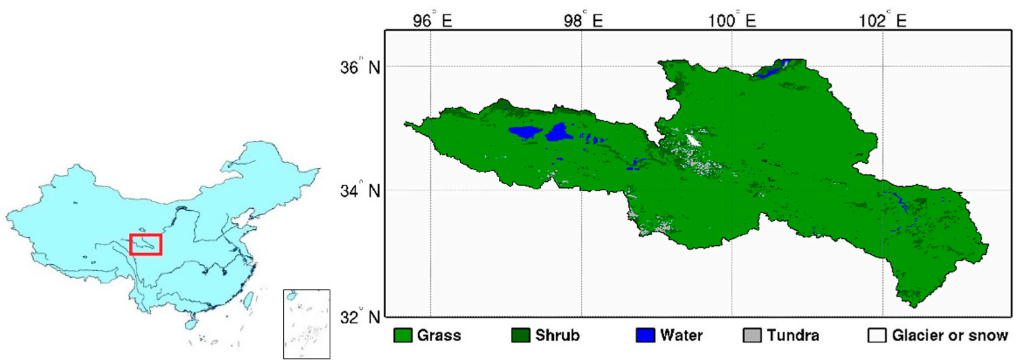

Figure 1. Location and land use of the Source Region of the Yellow River (SRYR).

The regular meteorological and eddy covariance observations from the SRYR Alpine Climate Stations (102°08′ E, 33°53′ N, 3443 m) were used from 1 August 2019. The underlying soil was alpine meadow soil, mainly covered by meadows with a height of 10 cm. The automatic meteorological station was set with three floors (1, 5, and 10 m), observing air temperature, air pressure, relative air humidity, surface temperature, wind speed at 10 m, precipitation, and sunshine hours. An eddy covariance system was erected at 3.02 m, with a frequency of 10 Hz, observing short-wave radiation flux and long-wave radiation flux (upward and downward), sensible heat flux, latent heat flux, soil heat flux (two layers: −10 cm and −20 cm). The system was set to output average flux every 10 min, and the results were finally averaged to obtain the hourly temporal scale data.

FY-2G and FY-3C are the geostationary meteorological and the polar-orbiting meteorological satellites, respectively, developed and operated by China. The Visible Infrared Spin Scan Radiometer carried by the FY-2G is the main earth observing instrument on the FY series satellites of the China Earth Observing System. It provides five channels of data from 1 July 2015. The resolution is 1.25 km for the visible channel, and 5 km for infrared and water vapor channels. The MicroWave Radiation Imager (MWRI) on FY-3C can be used for monitoring and research of soil moisture, snow cover, and ocean salinity. The sensor contains five frequencies-10.65, 18.7, 23.8, 36.5, and 89 GHz-and the corresponding spatial resolutions of sub-satellite points are 51 km, 85 km, 30 × 50 km, 27 × 45 km, 18 × 30 km, and 9 × 15 km. The data of the FY series satellites used in the study were all downloaded from the Fengyun Satellite Data Center (http://satellite.nsmc.org.cn/portalsite/default.aspx), including the 1-h average thermal infrared radiation brightness temperature and visible wide-band albedo, and MWRI 36.5 GHz microwave radiation brightness temperature. For specific processing steps, refer to the relevant literature [25].

In addition, the remote sensing data used in this study also included surface albedo, NDVI, LAI, and DEM. Surface albedo, NDVI, and LAI were obtained from MODIS (http://modis.gsfc.nasa.gov/). NDVI was adopted by the maximum value composite from an 8-day daily MODIS-NDVI, which eliminated the adverse effects of clouds, atmosphere, and satellite zenith angles. The DEM was obtained from the Shuttle Radar Topography Mission (SRTM) (http://srtm.csi.cgiar.org/), and its spatial resolution was 90 m. After the data or products were resampled to the nominal projection format of FY-2G, the final results were converted to the 0.078° longitude and latitude coordinate system to complete the drawing and statistical analysis.

Figure 2 shows the surface albedo, NDVI, and LAI in the SRYR retrieved by satellite remote sensing during the study period. The distribution figure shows that the surface albedo, NDVI, and LAI in the study area were highly consistent with its land use. Since the study area was dominated by alpine meadow grasslands, the surface albedo of the entire area was generally below 0.25. The minimum albedo (<0.10) occurred mainly in the west of the study area, indicating that there were large lakes, whereas the maximum value (>0.25) was in the northwest, indicating there was snow or permafrost tundra. The NDVI value in the area was between 0.45 and 0.85. Due to the distribution of lakes, certain areas also showed low values between 0.10 and 0.40. The value of LAI was between 0.9 and 2.1, indicating that although the distribution of vegetation presented certain spatial differences, there was no fundamental difference in general, and LAI had a more obvious spatial variation range than NDVI. The altitude in the region was around 3200–5200 m, and the location of the observation site was relatively flat. It should be noted that this research did not examine the surface ET of snow and lakes.

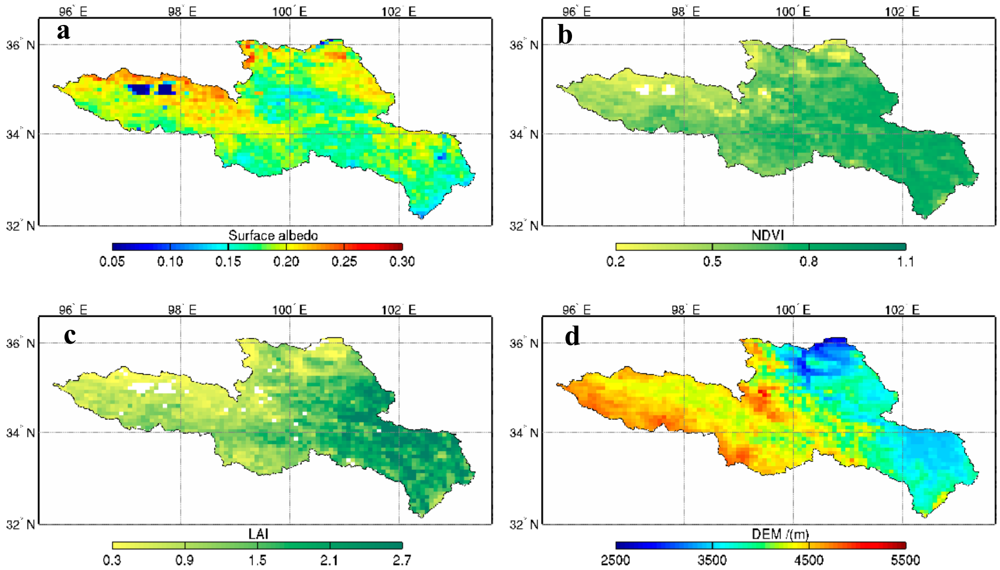

Figure 2. Surface parameters of the SRYR (**a**) Surface albedo (**b**) NDVI (**c**) LAI (**d**) DEM.

4. Results and Verification

4.1. Results of Energy Flux

Because the underlying surface of the study area was relatively flat and due to the footprint effect, the surface observation was of spatial representativeness from tens of meters to several kilometers. That means the energy flux from the surface observation can be approximately taken as the surface energy flux of the entire study area. To verify the satellite remote sensing algorithm and the estimated results, the field observations were compared with the estimated results. Figure 3 shows the daily variation of the near-surface energy flux in the SRYR retrieved by satellite remote sensing on 18 August 2019. The figure shows the hourly net radiation, soil heat flux, sensible heat flux, and latent heat flux from 11:00 to 16:00 Beijing time. The solar radiation absorbed by the ground after sunrise was greater than the expended radiation. At 11:00, the net radiation was about 400.0 Wm^{-2}, the soil heat flux was about 80.0 Wm^{-2}, the sensible heat flux was about 120.0 Wm^{-2}, and the latent heat flux value was about 200.0 Wm^{-2}; At midday, when the solar radiation strengthened, the net radiation continued to increase at 12:00 and 13:00, and the net radiation, soil heat flux, and sensible heat flux all reached the daily maximum at 12:00 and 13:00, which were about 650.0 Wm^{-2}, 100.0 Wm^{-2}, and 150.0 Wm^{-2}, respectively. The latent heat flux was about 300.0 Wm^{-2}. In the afternoon, when the solar radiation weakened, the net radiation continued to decrease at 14:00 and 15:00, to between 500.0 and 650.0 Wm^{-2}, although the study area showed relatively lower values at 15:00. The soil heat flux and sensible heat flux reached 60.0 Wm^{-2} and 100.0 Wm^{-2} at 15:00, respectively. The latent heat flux reached the daily maximum at 14:00 and decreased at 15:00, which were 320.0 Wm^{-2} and 250.0 Wm^{-2}, respectively. As the solar altitude, radiation and air saturation deficit weakened in the afternoon, the energy fluxes decreased at 16:00. The values of the energy fluxes at 16:00 were approximately similar to those at 12:00.

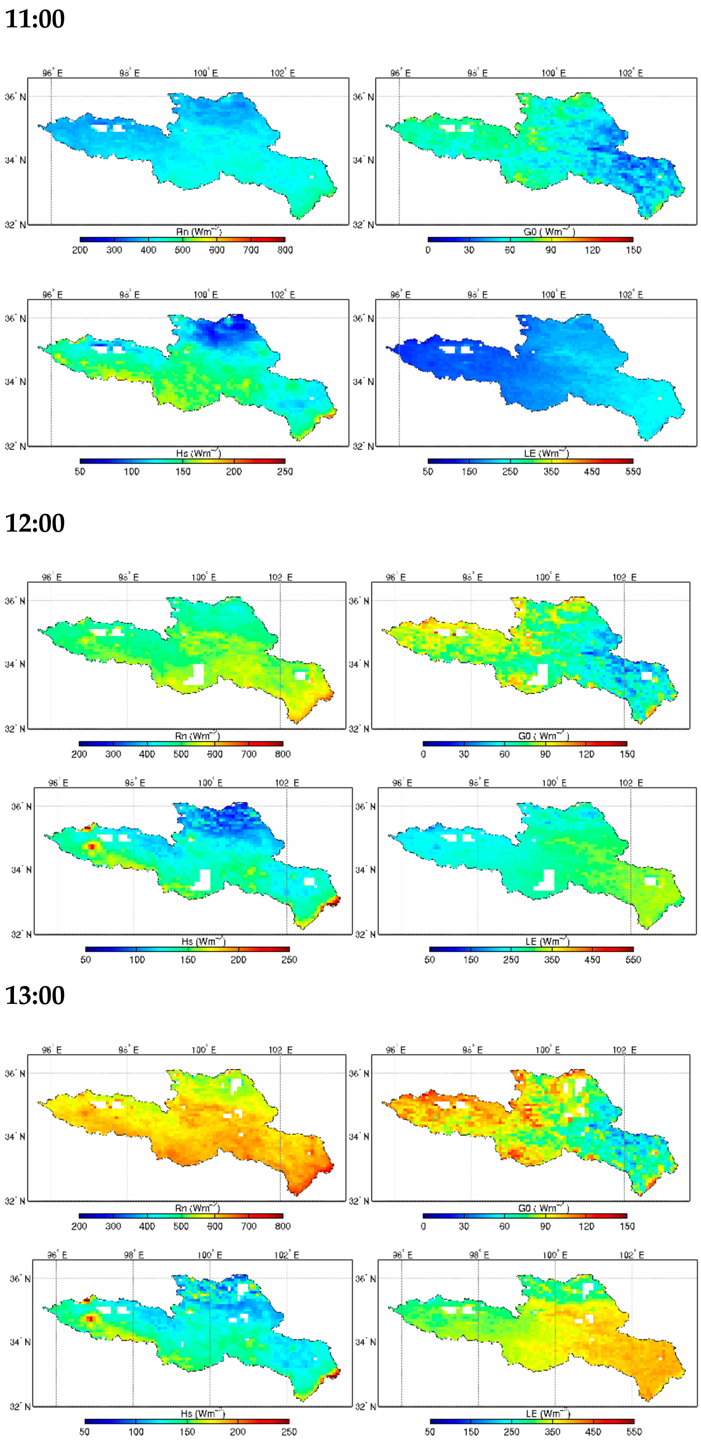

Figure 3. *Cont.*

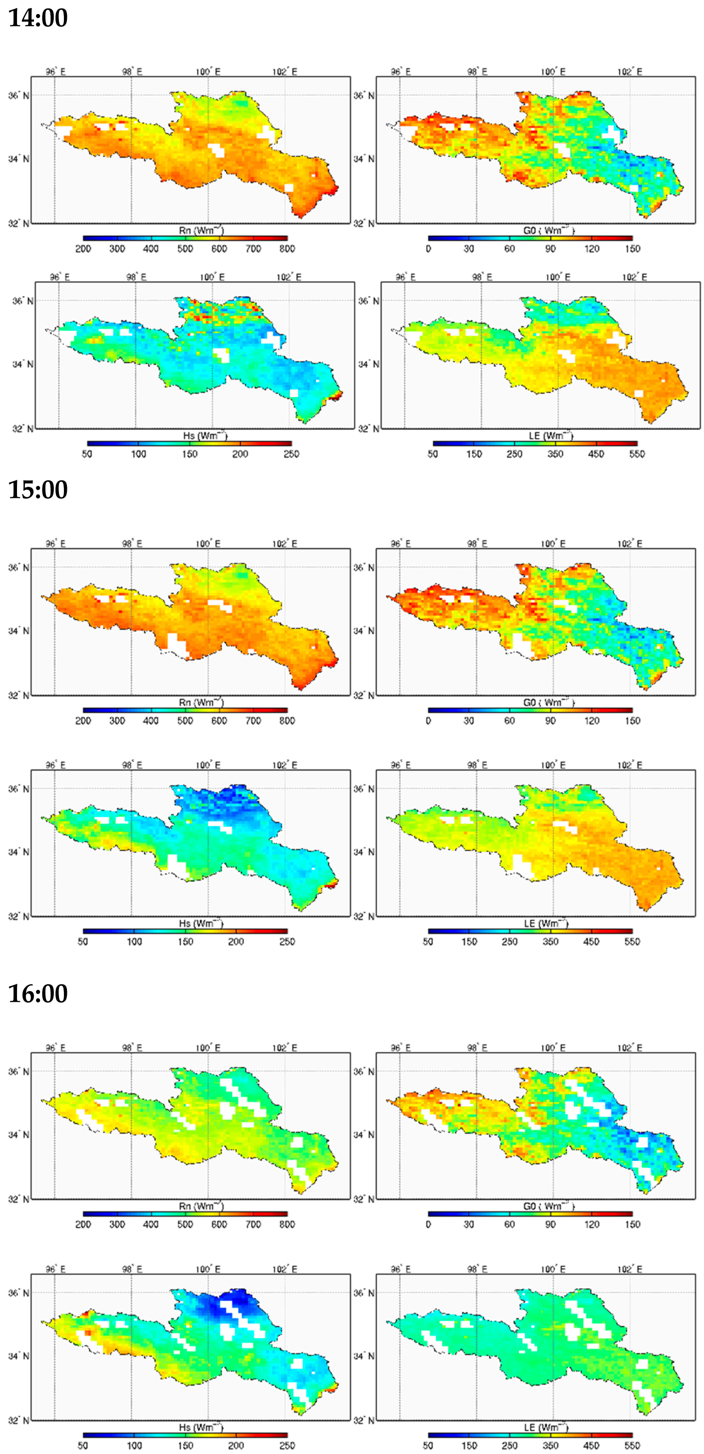

Figure 3. Hourly surface energy fluxes over the study area on 18 August 2019 (11:00 to 16:00 Beijing time).

From Figure 3, it can be seen that as the plateau convective cloud started to develop at 15:00, the near-infrared band of the geostationary satellite was affected by cloud cover, thus, the flux could not be retrieved in most of the area. However, the MWRI on the polar-orbiting satellite passed through the SRYR at around 15:40. Figure 4 shows the latent heat flux retrieved from the FY-3C MWRI and FY-2G visible/near-infrared data. The missing data over the cloud cover area from FY-2G was replaced with data from FY-3C. As shown in the figure, in areas with no cloud cover, the spatial distribution of high and low values retrieved by the two methods were basically consistent. Cloudy areas were mainly concentrated in the north and south of the study area, and the latent heat flux was about 200.0 Wm^{-2} (Figure 4b). However, the latent heat flux obtained from the visible and near-infrared band displayed sharp jumps in the cloudy area and its edge (Figure 4a), indicating that the results of the geostationary satellite obviously affected the retrieval results. The latent heat flux retrieved from the microwave was more continuous and smoother in the same area, and there were no jumps in edge regions (Figure 4b).

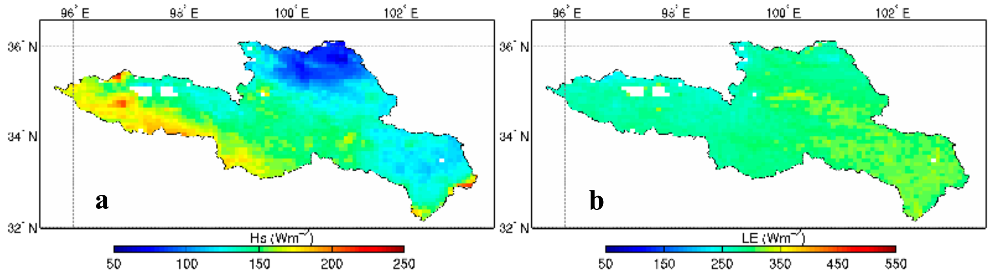

Figure 4. (**a**) Sensible heat flux from FY-2G and FY-3C (at Beijing time 15:40). (**b**) Latent heat flux from FY-2G and FY-3C (at Beijing time 15:40).

There was no significant difference in the spatial distribution of the retrieved latent heat fluxes between the two data sources. The two methods had specific advantages and disadvantages. Although the surface temperature retrieved by the FY-3C microwave was not affected by clouds, its resolution was about 25 km. The surface temperature retrieval needed to be spatially interpolated before being used, and the accuracy was slightly lower than that of the thermal infrared remote sensing. The polar-orbiting satellites observed variables instantaneously, whereas the geostationary satellites obtained one-hour average values.

4.2. Verification

Due to the footprint effect in the turbulence observations, the value observed by the eddy covariance system can not only be regarded as a value at a certain point but is of spatial representativeness from tens of meters to several kilometers. The time scale of the remote sensing was one hour, so the hourly observation data from the eddy covariance system were collected during the experiment to verify the estimated results. Figure 5 shows the comparisons between hourly surface energy flux measurements and the estimates on 18 August 2019, including net radiation flux, soil heat flux, sensible heat flux, and latent heat flux. The net radiation flux and sensible heat flux estimated by satellite remote sensing were compared with the ground measurements, and the root mean square error were 108.31 Wm^{-2} and 68 Wm^{-2} respectively; the root mean square error of the estimated soil heat flux and that obtained by the TCAV method was 14.28 Wm^{-2} and the root mean square error of the estimated latent heat flux and the ground measurement was 45.64 Wm^{-2}. The errors were all within a reasonable range.

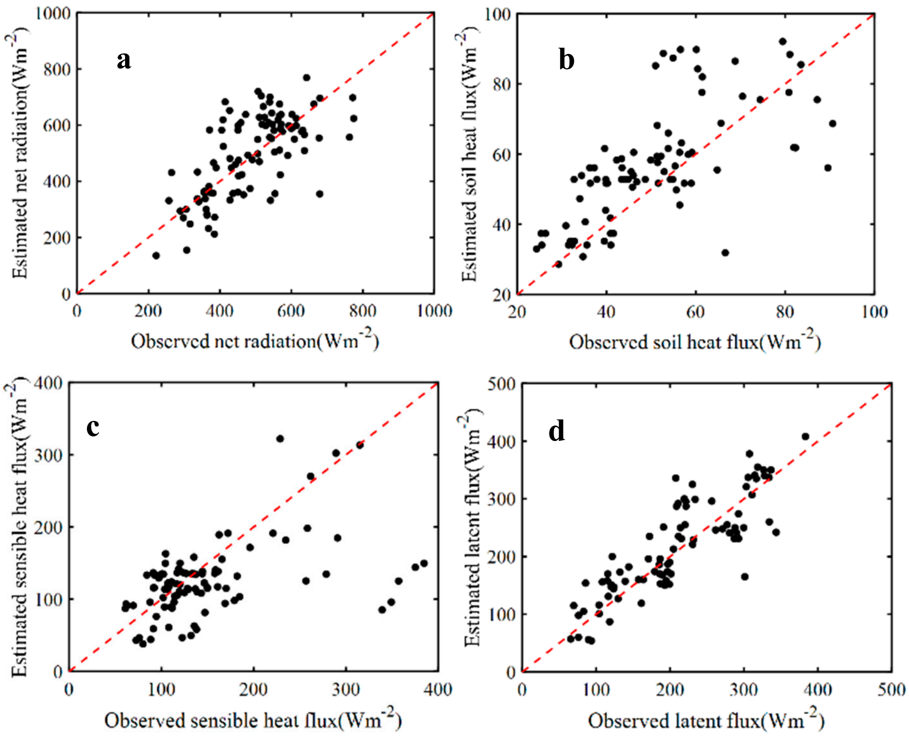

Figure 5. Comparisons between hourly surface energy flux measurements and the estimated: (**a**) net radiation, (**b**) soil heat flux, (**c**) sensible heat flux, (**d**) latent heat flux.

5. Discussions

5.1. The Relationship between the Conditional Expectation and the Temperature

Surface temperature is the most direct feedback of the surface to meteorological conditions and is one of the key factors affecting the net radiation distribution on the surface. The surface temperature and energy distribution showed certain relationships at the spatial scale due to the climate and land cover of the study area. The spatially conditional expectation of the surface energy components and surface temperature retrieved by remote sensing was derived and analyzed after smoothing (Figure 6a). The trend line was smoothed. The results show that the distribution of net radiation generally displayed a similar trend to that of sensible heat. From a starting point of 275 K, with the increase in temperature, the conditional expectations of net radiation and latent heat flux increased, until stabilizing at 298–301 K, and decreasing after 302 K. Sensible heat flux showed an upward trend from 275 to 288 K, but decreased slowly after 288 K. In general, the expected values of sensible heat, net radiation and latent heat flux from 275 to 280 K were consistent, showing an upward trend. However, starting from 290 K, the expected value of sensible heat decreased slightly, while the expected latent heat increased. The expected value of soil heat flux increased slowly. Therefore, in mid-August, the daily surface sensible heat flux in the SRYR over the Qinghai-Tibet Plateau rose with the increase in temperature below 288 K. The sensible heat flux changed slightly within the temperature range of 280–285 K, and the latent heat flux increased significantly between 280 and 298 K.

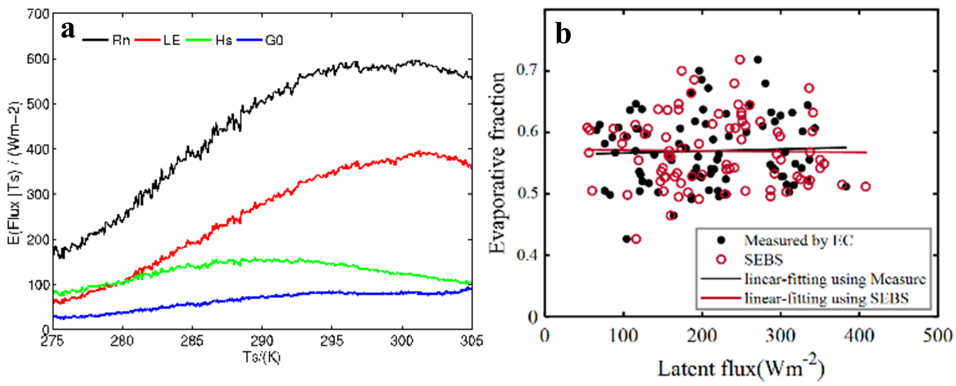

Figure 6. (**a**) Trend of energy fluxes conditional expectation with the land surface temperature. (**b**) Relationship between evaporation fraction (EF) and latent heat flux.

The above analysis shows that under the abundant surface soil moisture conditions, with the increase in temperature and net radiation, the effective energy distribution of the surface changed significantly with the increase in temperature; in particular, when the surface temperature exceeded 290 K, the effective energy was mainly used for surface ET. This also indicates that, when the surface temperature exceeded 290 K, its retrieval accuracy had a significant impact on the ET retrieval, i.e., the higher the surface temperature, the greater the ET retrieval error.

5.2. The Relationship between Evaporation Fraction, Latent Heat Flux, and Daily ET

The evaporation fraction represented the energy exchange between the lower atmosphere and the near-surface at a regional scale, that is, the distribution of effective energy between surface sensible heat and latent heat flux. Under ideal conditions, when the soil was at its dry limit and the soil moisture was not available for evaporation, the latent heat flux was approximately zero and the sensible heat flux reached its maximum. In the wet limit environment, in which the soil moisture was sufficient, the latent heat flux reached its maximum. The First ISLSCP Field Experiment (FIFE) indicated that the evaporation fraction remained relatively stable under typical clear sky conditions, with the exception of mornings and evenings, so the ET throughout the day could be derived from the evaporation fraction at a certain moment and the surface effective energy of the whole day [26,27]. The observation from geostationary satellites made it possible to obtain the hourly scale evaporation fraction by remote sensing and provided a data source for verification of the hourly scale evaporation fraction using the eddy covariance observation system.

Figure 6b presents the retrieved and observed latent heat flux and evaporation fraction at an hourly scale. Although the evaporation fractions of the two were similar, with values between 0.51 and 0.65, the fitting straight line showed different trends. The observed evaporation fraction showed a more obvious trend of decreasing with the increase in latent heat flux, whereas the retrieved evaporation fraction displayed a slight increase. The two lines intersected when the latent heat flux was 210.19 Wm^{-2}. However, due to the lack of accurate model-driven and surface verification data-sets, which leads to errors in the model forcing field and uncertainty of the model parameters, model calibration and error analysis based on land surface observations was complicated. More importantly, SEBS is a closure energy model, which retrieves surface ET based on the energy residual method, whereas the eddy covariance system used by the station for surface flux observation is not closed, however, and is still widely used for surface ET observation.

The evaporation fraction was evaluated using the observations from the eddy covariance system and the retrievals from the remote sensing data. At 12:00, the observed evaporation fraction was the closest to the estimated evaporation fraction. Hence, 12:00 was defined as the analysis time. The retrieved evaporation fraction at this time was 0.57, which was considered to be the effective evaporation fraction of the day. The daily ET calculated based on this value was 4.85mm, and the value of the total ET derived from the evaporation fraction at other times was within the range of 4.04–5.25 mm. Compared with the cumulative value, the daily ET derived from the effective evaporation fraction was closer to the observed value with the same input forcing and the model physics schemes. Therefore, the evaporation fraction at 12:00 was used to obtain the daily ET and this method was able to eliminate the retrieval error at a certain moment without destroying the physical mechanism of the retrieval model. The method has the potential to become an effective means of retrieving ET using geostationary satellite observations.

5.3. Daily ET

The spatial distribution of daily ET on 18 August 2019 in the SRYR was obtained by collecting the evaporation fraction and accumulating the hourly latent heat flux (Figure 7). The regional ET was between 2.0 and 4.0 mm. The low-value area appeared in the north of the study area with ET below 2.5 mm. The maximum daily ET was about 4.0 mm in the southeast of the SRYR, indicating that the surface soil water, vegetation, water available for ET, and meteorological conditions were all conducive to ET. In contrast, the northern part of the study area is located at the northern foot of Tanggula Mountain, which is not favorable for energy transfer from the surface to the atmosphere due to the high altitude and harsh weather conditions.

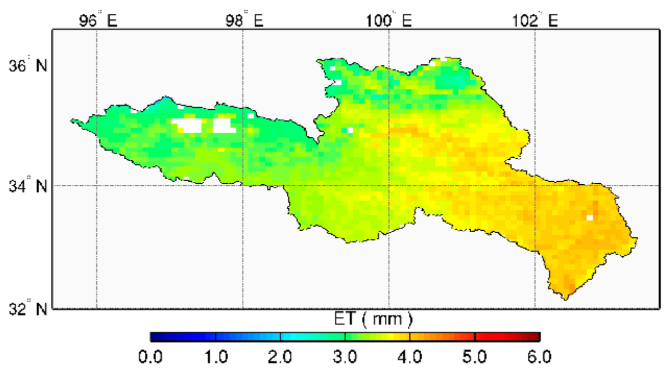

Figure 7. Spatial distribution of daily evapotranspiration (ET) over Northern Tibetan Plateau on 18 August 2019.

6. Conclusions

In this research, the spatial distribution of energy fluxes and daily ET at different times of the day in the SRYR were estimated using the SEBS algorithm and ground meteorological observation data, combined with the data of visible/near-infrared and microwave observations from the Fengyun series of meteorological satellites. Considering the influence of convective clouds during the afternoon above the plateau, which prevents visible and near-infrared observation in cloud-cover conditions, we used the MWRI brightness temperature to estimate the surface temperature. The hourly change of latent heat flux presented a sound unimodal diurnal variation. As the solar radiation increased after sunrise, the latent heat flux gradually increased from 180.0 Wm^{-2} at 11:00 to 200.0 Wm^{-2} at 12:00. The latent heat flux was about 280.0 Wm^{-2} at 13:00. At 14:00, the value reached its daily maximum of around 350.0 Wm^{-2}, and in some areas reached 400.0 Wm^{-2}. As the solar altitude, radiation, and air saturation deficit weakened in the afternoon, at 16:00, we adopted the surface temperature retrieved from the microwave data and found the latent heat flux in the cloud-free area was about 280.0 Wm^{-2}, and the cloud-covered area 150.0 Wm^{-2}. Converting the latent heat flux to the actual land surface ET, it was found that the daily ET in most of the study area was between 2.0 mm and 4.0 mm. The results were within a reasonable error range and lay a foundation for realizing the commercialization of land surface ET in the future.

The focus of this research was to investigate the hourly retrieval of ET using satellite remote sensing data. Due to the limitations of ground observation data and the overpass time of polar-orbiting satellites, the accuracy of the algorithm under cloud cover was not further analyzed. In addition, cloud-free and cloud-covered represent theoretical conditions, and cloud total amount (CTA) was obtained using the radiation transfer equation and the data from the visible and near-infrared channels. This could be used to determine whether the study area at the regional scale was under cloud cover, but the accuracy of determining whether a single spot was affected by cloud cover was yet to be considered. In the next step, it will be necessary to take manual field observation experiments, that is, to record the cloud amount at the observation spot for each moment, and analyze the difference between the measured ET and the estimated results under cloud cover. The focus will be to improve the estimation accuracy of the model under cloud cover for a more reliable estimate of regional ET under all weather conditions.

Author Contributions: Conceptualization and writing—original draft preparation R.L. supervision, J.W.; investigation, X.W.; formal analysis, Z.W. and Y.L.; software, M.Z. All authors have read and agreed to the published version of the manuscript.

Funding: This research was funded by supported by The Second Tibetan Plateau Scientific Expedition and Research (STEP) program (grant no. 2019QZKK0105); National Natural Science Foundation of China, grant number 42075065, 91737103, 41530529.

Institutional Review Board Statement: Not applicable.

Informed Consent Statement: Not applicable.

Data Availability Statement: Not applicable.

Acknowledgments: Special thanks are given to the anonymous reviewers who greatly helped to improve the quality of the manuscript.

Conflicts of Interest: The authors declare no conflict of interest.

References

1. Priestley, C.H.B.; Taylor, R.J. On the assessment of surface heat flux and evaporation using large-scale parameters. *Mon. Weather Rev.* **1972**, *100*, 81–92. [CrossRef]
2. Wang, K.C.; Dickinson, R.E. A review of global terrestrial evapotranspiration: Observation, modeling, climatology, and climatic variability. *Rev. Geophys.* **2012**, *50*. [CrossRef]
3. Kim, N.; Kim, K.; Lee, S.; Cho, J.; Lee, Y. Retrieval of daily reference evapotranspiration for croplands in South Korea using machine learning with satellite images and numerical weather prediction data. *Remote Sens.* **2020**, *12*, 3642. [CrossRef]
4. Su, Z.; Schmugge, T.; Kustas, W.P.; Massman, W.J. An evaluation of two models for estimation of the roughness height for heat transfer between the land surface and the atmosphere. *J. Appl. Meteorol.* **2001**, *40*, 1933–1951. [CrossRef]
5. Nedbal, V.; Láska, K.; Brom, J. Mitigation of arctic tundra surface warming by plant evapotranspiration: Complete energy balance component estimation using LANDSAT satellite data. *Remote Sens.* **2020**, *12*, 3395. [CrossRef]
6. Cleugh, H.A.; Lenning, R.; Mu, Q. Regional evaporation estimates from flux tower and MODIS satellite data. *Remote Sens. Environ.* **2007**, *106*, 285–304. [CrossRef]
7. Mu, Q.; Heinsch, F.; Zhao, M.; Running, S. Development of a global evapotranspiration algorithm based on MODIS and global meteorology data. *Remote Sens. Environ.* **2007**, *111*, 519–536. [CrossRef]
8. Jackson, R.D.; Reginato, R.J.; Idso, S.B. Wheat canopy temperature: A practical tool for evaluating water requirements. *Water Resour. Res.* **1977**, *13*, 651–656. [CrossRef]
9. Allen, R.G.; Tasumi, M.; Trezza, R. Satellite-based energy balance for mapping evapotranspiration with internalized calibration (METRIC)-model. *J. Irrig. Drain. Eng.* **2007**, *133*, 380–394. [CrossRef]
10. Carpintero, E.; Mateos, L.; Andreu, A.; González-Dugo, M.P. Effect of the differences in spectral response of Mediterranean tree canopies on the estimation of evapotranspiration using vegetation index-based crop coefficients. *Agric. Water Manag.* **2020**, *238*, 106201. [CrossRef]
11. Jiang, L.; Islam, S. A methodology for estimation of evapotranspiration over large areas using remote sensing information. *Geophys. Res. Lett.* **1999**, *26*, 2773–2776. [CrossRef]
12. Bastiaanssen, W.G.M.; Menenti, M.; Feddes, R.A.; Holtslag, A.A.M. A remote sensing surface energy balance algorithm for land (SEBAL): 1. Formulation. *J. Hydrol.* **1998**, *212–213*, 198–212. [CrossRef]
13. Roerink, G.J.; Su, Z.; Menenti, M. A simple remote sensing algorithm to estimate the surface energy balance. *Phys. Chem. Earth* **2000**, *25*, 147–157. [CrossRef]
14. Su, Z. The surface energy balance system (SEBS) for estimation of turbulent heat fluxes. *Hydrol. Earth Syst. Sci.* **2002**, *6*, 85–99. [CrossRef]
15. Allen, R.G.; Tasumi, M.; Morse, A. *Satellite-Based Evapotranspiration by METRIC and Landsat For Western States Water Management*; US Bureau of Reclamation Evapotranspiration Workshop: Fort Collins, CO, USA, 2005.

16. Shuttleworth, W.J.; Wallace, J.S. Evaporation from sparse crops-an energy combination theory. *Q. J. R. Meteorol. Soc.* **1985**, *111*, 839–855. [CrossRef]
17. Norman, J.M.; Kustas, W.P.; Humes, K.S. Source approach for estimating soil and vegetation energy fluxes in observations of directional radiometric surface temperature. *Agric. For. Meteorol.* **1995**, *77*, 263–293. [CrossRef]
18. Chen, S.; Liu, W.H.; Ye, T. Dataset of trend-preserving bias-corrected daily temperature, precipitation and wind from NEX-GDDP and cmIP5 over the Qinghai-Tibet Plateau. *Data Brief.* **2020**, *31*, 105733. [CrossRef]
19. Chen, X.L.; Su, Z.; Ma, Y.M.; Yang, K.; Wang, B. Estimation of surface energy fluxes under complex terrain of Mt. Qomolangma over the Tibetan Plateau. *Hydrol. Earth Syst. Sci.* **2013**, *17*, 1607–1618. [CrossRef]
20. Brutsaert, W. On a derivable formula for long-wave radiation from clear skies. *Water Resour. Res.* **1975**, *11*, 742–744. [CrossRef]
21. Liu, R.; Wen, J.; Wang, X.; Zhang, Y. Evapotranspiration estimated by using datasets from the Chinese FengYun-2D geostationary meteorological satellite over the Yellow River source area. *Adv. Space Res.* **2015**, *55*, 60–71. [CrossRef]
22. Li, X.Q.; Yang, H.; You, R. Remote sensing typhoon Songda's rainfall structure based on Microwave Radiation Imager of FY-3B satellite. *Chin. J. Geophys.* **2013**, *28*, 875–889. (In Chinese)
23. Han, C.; Ma, Y.; Chen, X.; Su, Z. Trends of land surface heat fluxes on the Tibetan Plateau from 2001 to 2012. *Int. J. Clim.* **2017**, *37*. [CrossRef]
24. Gao, Q.; Wang, S.; Yang, X. Estimation of surface air specific humidity and air–sea latent heat flux using FY-3C microwave observations. *Remote Sens.* **2019**, *11*, 466. [CrossRef]
25. Niu, Z.; Zou, X.; Ray, P.S. Development and testing of a clear-sky data selection algorithm for FY-3C/D microwave temperature sounder-2. *Remote Sens.* **2020**, *12*, 1478. [CrossRef]
26. Xu, Z.; Liu, S.; Xu, T. The observation and calculation method of soil heat flux and its impact on the energy balance closure. *Adv. Earth Sci.* **2013**, *28*. [CrossRef]
27. Shuttleworth, W.J.; Gurney, R.J.; Hsu, A.Y. FIFE: The variation in energy partition at surface flux sites. *Remote Sens. Large Scale Glob. Process.* **1989**, *186*, 67–74.